Assessment of target detection limits in hyperspectral data

Gross, Wolfgang ; Boehler, Jonas ; Schilling, Hendrik ; Middelmann, Wolfgang ; Weyermann, Jörg ; Wellig, Peter ; Oechslin, Roland ; Kneubühler, Mathias

Abstract: Hyperspectral remote sensing data can be used for civil and military applications to detect and classify target objects that cannot be reliably separated using broadband sensors. The comparably low spatial resolution is compensated by the fact that small targets, even below image resolution, can still be classiffed. The goal of this paper is to determine the target size to spatial resolution ratio for successful classiffcation of different target and background materials. Airborne hyperspectral data is used to simulate data with known mixture ratios and to estimate the detection threshold for given false alarm rates. The data was collected in July 2014 over Greding, Germany, using airborne aisaEAGLE and aisaHAWK hyperspectral sensors. On the ground, various target materials were placed on natural background. The targets were four quadratic molton patches with an edge length of 7 meters in the colors black, white, grey and green. Also, two different types of polyethylene (camouage nets) with an edge length of approximately 5.5 meters were deployed. Synthetic data is generated from the original data using spectral mixtures. Target signatures are linearly combined with different background materials in specific ratios. The simulated mixtures are appended to the original data and the target areas are removed for evaluation. Commonly used classiffcation algorithms, e.g. Matched Filtering, Adaptive Cosine Estimator are used to determine the detection limit. Fixed false alarm rates are employed to find and analyze certain regions where false alarms usually occur first. A combination of 18 targets and 12 backgrounds is analyzed for three VNIR and two SWIR data sets of the same area.

DOI: https://doi.org/10.1117/12.2192197

Assessment of target detection limits in hyperspectral data

Gross W.[a], Boehler J.[b], Schilling, H.[a], Middelmann W.[a], Weyermann J.[b], Wellig P.[c], Oechslin R.[c] and Kneubuehler M.[b]

[a]Fraunhofer Institute of Optronics, System Technologies and Image Exploitation IOSB, Gutleuthausstrasse 1, D-76275 Ettlingen, Germany;
[b]Remote Sensing Laboratories, University of Zurich, Winterthurerstrasse 190, CH-8057 Zurich, Switzerland;
[c]Science and Technology Department, armasuisse, Feuerwerkerstasse 39, CH-3602 Thun, Switzerland

ABSTRACT

Hyperspectral remote sensing data can be used for civil and military applications to detect and classify target objects that cannot be reliably separated using broadband sensors. The comparably low spatial resolution is compensated by the fact that small targets, even below image resolution, can still be classified. The goal of this paper is to determine the target size to spatial resolution ratio for successful classification of different target and background materials. Airborne hyperspectral data is used to simulate data with known mixture ratios and to estimate the detection threshold for given false alarm rates. The data was collected in July 2014 over Greding, Germany, using airborne aisaEAGLE and aisaHAWK hyperspectral sensors. On the ground, various target materials were placed on natural background. The targets were four quadratic molton patches with an edge length of 7 meters in the colors black, white, grey and green. Also, two different types of polyethylene (camouflage nets) with an edge length of approximately 5.5 meters were deployed. Synthetic data is generated from the original data using spectral mixtures. Target signatures are linearly combined with different background materials in specific ratios. The simulated mixtures are appended to the original data and the target areas are removed for evaluation. Commonly used classification algorithms, e.g. Matched Filtering, Adaptive Cosine Estimator are used to determine the detection limit. Fixed false alarm rates are employed to find and analyze certain regions where false alarms usually occur first. A combination of 18 targets and 12 backgrounds is analyzed for three VNIR and two SWIR data sets of the same area.

Keywords: Hyperspectral, detection limit, target to background ratio, subpixel classification, synthetic data

1. INTRODUCTION

The goal to determine target-to-background detection limits for hyperspectral data is difficult using real remote sensing data. Specific experimental setups are required to have a representative combination of targets, background and target sizes. Also, the task is difficult to evaluate. Multiple conditions must be kept in mind if real remote sensing data is used. The experimental setup, especially for detection of subpixel targets, requires accurate ground truth measurements for GPS positions. Additionally, the targets should not be placed directly next to other objects, like trees or buildings, where multiple reflections might affect the spectral signature. While planning the flight it is important to keep in mind that the target might not be pictured in a single pixel even though it is smaller than the image resolution. Instead it can be spread over up to four pixels, each containing only a small amount of target. Multiple flight lines should be performed to make sure there exists at least one flight line where the specific target is completely included in a single pixel. However, it is hard to assess during the data recording if the previous condition is met. Also, inaccurate georeferencing makes assessment difficult. On the sensor side, frame rate and exposure per frame play an important role. The point spread function of the sensor during flight depends on the exposure and smearing of spectral information occurs.[1] In the practical approach we used large molton sheets of 7 x 7 meters during our measurement campaign in 2014 in Greding,

Send correspondence to W. Gross
E-mail: wolfgang.gross@iosb.fraunhofer.de

Target and Background Signatures, edited by Karin U. Stein, Ric H. M. A. Schleijpen, Proc. of SPIE Vol. 9653, 96530J
 · doi: 10.1117/12.2192197

Germany.
The original idea was similar to the edge unmixing from Kerekes[2] to interpolate the ratio per pixel by following a straight line along the edges of the molton sheets. The GPS positions of the edges of each sheet were accurately measured. It was planned to georeference the hyperspectral data to these GPS positions and approximate the target-to-background ratio along the edges. However, it turned out to be impossible to manually select suitable tie points for the georeferencing process such that the corners of each molton sheet in the images aligned with the corresponding GPS positions. The reason was the high amount of smear in the data that caused the sheets to appear larger than their physical shape on the ground. Also, the surface was not completely level and the background was not homogeneous enough for our experiments. Thus, it was not possible to calculate accurate target-to-background ratios and it was necessary to switch to simulated data generated from the original data sets.
With our simulation process from section 3 and the calculated results in section 4 it is possible to approximate detection limits for different target and background combinations.

2. OBJECTIVE AND CLASSIFIERS

The scope of this paper are the following objectives:

- Approximate the mean detection limit for different algorithms and target/background combinations
- Analyze the change of detection limits with reduced reflectance by comparing the results of *Molton (white)*, *Molton (grey)* and *Molton (black)*
- Analyze the change of detection limit with respect to the background material, e.g. comparing *Molton (green)* mixed with *Grass (long/short)*, *Tree (dark/bright)* or *Asphalt*

For the evaluation we use real hyperspectral remote sensing data appended with linear mixtures of specific target and background spectra taken from these data sets. The next step is to use target spectra as input for a number of commonly used classification algorithms that are introduced in this section. Finally, the detection limit with respect to a specified false alarm rate is calculated for each combination.
We use the following notation to describe the different classifiers: Let $V \in \mathbb{R}^{n \times N}$ be the hyperspectral data set with n spectral bands and N samples. As none of the used classifiers require neighborhood information we are able to reorganize the 3D data cube in this way to switch to matrix operations. Let $t \in \mathbb{R}^n$ be the n-dimensional vector of the spectral target signature and $x \in \mathbb{R}^n$ be a sample spectrum from the data set V. $\Sigma \in \mathbb{R}^{n \times n}$ is the covariance matrix of V, also referred to as background covariance matrix as we removed all target areas from the data to not disturb the statistics. Finally, $\mu \in \mathbb{R}^n$ is the mean background vector and $\widetilde{t} = t - \mu$ and $\widetilde{x} = x - \mu$ are the centralized target and sample vectors. The output of each classifier is a similarity value per sample x. A subsequent binary classification can be done by a nearest neighbor approach when more than one target is used. In our case only one target signature is used at a time and a threshold to the similarity images is applied to enforce a desired false alarm rate.

2.1 Spectral Angle Mapper

The Spectral Angle Mapper (SAM) is the most intuitive to understand among the number of classifiers we chose to estimate the detection limits.[3] It calculates the angle between a given target spectrum and each spectrum in the scene by treating them as vectors by

$$\mathrm{SAM}\,(x) = \arccos \frac{\langle x, t \rangle}{\|x\|_2 \, \|t\|_2}.$$

The SAM algorithm is insensitive to illumination as it only uses the vectors direction and not the vectors length. However, nonlinear effects in the data impair the calculation. It is mostly used as a first approach as it is computationally cheap and does not require image statistics. Classifying by the spectral angle is usually used as a first approach to calculate a segmentation of images with large homogeneous areas. It is useful specifically for mineralogical exploration as there is little material variation compared to vegetation. For multiple target spectra, a similarity image is calculated for each target and the class labels can be determined by a k-Nearest Neighbor calculation.

2.2 Matched Filter

The Matched Filter (MF) is based on binary hypothesis testing.[4] The likelihood ratio can be calculated as the ratio of the conditional probability density functions

$$\Lambda(x) = \frac{p(x|\text{target present})}{p(x|\text{target absent})}. \tag{1}$$

If $\Lambda(x)$ is larger than a given threshold, the hypothesis for "target present" is accepted. The probability density functions for each hypothesis can be modeled as normal distributions. Since the amount of target pixels in the image is very small we can assume that the covariance matrix $\Sigma \in \mathbb{R}^{n\times n}$ holds for both hypotheses. Then, we can maximize the cost function (1) to get an adaptive matched filter that suppresses clutter based on background statistics. In practice we calculate the MF for a sample x as

$$\text{MF}(x) = \frac{\widetilde{t}^T\Sigma^{-1}\widetilde{x}}{\widetilde{t}^T\Sigma^{-1}\widetilde{t}}.$$

2.3 Constrained Energy Minimization

The idea behind Constrained Energy Minimization (CEM) is that a finite impulse response filter is used to filter the data by looking for desired target signatures while simultaneously suppressing background information.[4] The background covariance matrix is exploited to characterize the composite unknown background. Thus, the response of the known target signature is maximized. Calculation of CEM is as follows:

$$\text{CEM}(x) = \frac{t^T\Sigma^{-1}x}{t^T\Sigma^{-1}t}.$$

Mathematically, the difference between MF and CEM is the centering by the background means μ.

2.4 Generalized Likelihood Ratio Test

The Generalized Likelihood Ratio Test (GLRT) is a decision rule to detect a signal with unknown amplitude masked by Gaussian interference.[5] GLRT also assumes knowledge of background statistics in the form of a covariance matrix Σ. To confer a sense of optimality to GLRT, work by Scharf and Friedlander shows equivalence between GLRT and uniformly most powerful detectors.[6] Also, the property of constant false alarm rate (CFAR) holds for GLRT, which implies that the probability of a false alarm is independent of the background covariance matrix. The calculation is done by

$$\text{GLRT}(x) = \frac{\left(\widetilde{t}^T\Sigma^{-1}\widetilde{x}\right)^2}{\widetilde{t}^T\Sigma^{-1}\widetilde{t}\,(1+\widetilde{x}^T\Sigma^{-1}\widetilde{x})}.$$

2.5 Adaptive Coherence Estimator

The Adaptive Coherence Estimator (ACE) is very similar to GLRT. Calculation is done by

$$\text{ACE}(x) = \frac{\left(\widetilde{t}^T\Sigma^{-1}\widetilde{x}\right)^2}{\left(\widetilde{t}^T\Sigma^{-1}\widetilde{t}\right)(\widetilde{x}^T\Sigma^{-1}\widetilde{x})}.$$

It is invariant to relative scaling of test and training data and also satisfies the CFAR condition. ACE has a different approach to stretching the detection statistics compared to GLRT and, thus, achieves a better target to background separation. This facilitates the selection of a suitable decision threshold. In Chapter 4, it can be seen that ACE was most often the algorithm providing the best results. Although there are several occasions where GLRT performed equally good, the contrast in the resulting classification similarity image was better for ACE.

2.6 Spectral Information Divergence

The Spectral Information Divergence (SID) is a method to measure spectral similarity and discriminability. It also works better than SAM when only a fraction of the target material is contained in a given pixel.[7] Spectra are treated as random variables and the SID measures the discrepancy of probabilistic behaviors between a given target signature and a sample spectrum from the data as follows

$$\mathrm{SID}(x) = D\left(x||t\right) + D\left(t||x\right) = \left|\sum_{i=1}^{n} x_i \log\left(x_i/t_i\right)\right| + \left|\sum_{i=1}^{n} t_i \log\left(t_i/x_i\right)\right|.$$

$D\left(x||t\right)$ is essentially the relative entropy of t with respect to x.

2.7 Orthogonal Subspace Projection

The Orthogonal Subspace Projection (OSP) is the only method we used that exploits background spectra to better discriminate between target and background. Using these it generates a subspace to annihilate any response of non-targets. After that a matched filter is used to find spectra that are similar to the projected target spectrum.[4] The method we used for our experiment is slightly altered from the original by introducing a scaling so that the results can also be used for abundance estimation. It can be written as

$$\mathrm{OSP}(x) = \frac{t^t P_B^{\perp} x}{t^T P_B^{\perp} t},$$

where

$$P_B^{\perp} = I - U(U^T U)^{-1} U^T,$$

with I the identity matrix and U the matrix of background spectra.
For the experiments in this paper we set U to contain all the previously determined background spectra that we also used to generate the simulated data.

3. EXPERIMENTAL SETUP

In preparation of the simulation process three flight lines of aisaEagle (VNIR: visible and near infrared, 128 bands, $390 - 990$ nm) and two lines of aisaHawk (SWIR: short wave infrared, 239 bands, $990 - 2500$ nm) data were identified to picture all targets. The disparity in the amount of flight lines per sensor is an effect of different field of views. The data was radiometrically, geometrically and atmospherically corrected and has a ground sampling distance of 0.5 m in the VNIR and 1.0 m SWIR respectively. The spatial resampling was done with nearest neighbor interpolation to prevent changes in the spectral signatures. As the automatic georeferencing was only accurate by 0.5 pixels, regions of interest (ROI) for each target and the selected background areas were determined manually.
Targets beside molton sheets of different color were two types of camouflage net, a tank and an inflatable tank decoy. The camouflage nets were evaluated separately to account for slight differences in pattern. Also, one net was frequently watered to check if it affects the detection. The molton sheets were 7 x 7 m big in four different colors: black, grey, white and green. Although the colors are different, the base spectral signatures of the fabric are very similar above 670 nm. The features in these wavelength range are proportional to the norm of each spectrum. Also, their surface is completely homogeneous and reflectance should closely model that of a Lambertian surface.
Figures 1 and 2 depict color composites of one of the VNIR and SWIR data sets. The left rectangle contains the area with camouflage nets, the right contains the four molton patches.
The synthetic data was generated using linear mixtures of target and background spectra. For each data set and each combination of target and background materials a new synthetic data set was computed. All target areas were cut out as depcited in Figure 3 with a safety margin of 10 pixels in the VNIR data, and 5 pixels in the SWIR respectively. This was done to not confuse any remaining parts of the original targets as false alarms during the evaluation process. Also, the data set without targets is used to calculate image statistics for the classifiers, mainly the background covariance matrix Σ, as the basic assumption is that only a small part of an

Figure 1. RGB color composite of VNIR data set used for simulation. Left rectangle contains the sets of camouflage nets, containing 6 nets in total and three of each type, right rectangle contains the 4 molton sheets.

Figure 2. False color composite image of SWIR data set used for simulation. Left rectangle contains the sets of camouflage nets, containing 6 nets in total and three of each type, right rectangle contains the 4 molton sheets. The black area comes from the different field of view of the sensors and is not used for classification/evaluation.

area is covered by target materials and the effect of a few pixels on the image statistic is negligible.
As we require numerous target-to-background ratios, it is easier to use this approach than to calculate a new data set for each ratio. For each pixel of a given target, linear spectral mixtures with a selection of 20 pixels of each background material are calculated. The mixture ratios are chosen such that the amount of mixed spectra matches the number of lines of the data set. The synthetic data can then be appended to the image by continuing the data set with as many columns as the number of target pixels multiplied by the number of background pixels. Each simulated column ranges from 100 % target pixel and 0 % background at the bottom to 0 % target and 100 % background on the top.
The target masks were manually selected to only contain pixels that were considered to be pure target spectra. For the background masks homogeneity is not specifically enforced. It is more important to not mix different conditions like *Grass (long)* and *Grass (short)* that possess separate specific features. The number of pixels per target ranges from 5 to 30 and we use each to compute the mixtures. The background areas are generally larger with $100 - 500$ pixels, which makes it too expensive to use all of them at once. Instead, 20 background pixels are selected by calculating a histogram with 20 bins over the norm of all background spectra and selecting the spectral signature closest to the mean value in each bin. An example for the resulting synthetic VNIR data for the mixture of *Molton (green)* with *Asphalt* is depicted in Figure 3. As molton is homogeneous the mixtures

Figure 3. RGB color composite of simulated VNIR data for the mixture of *Molton (green)* with *Asphalt*. Black areas in the original scene are the cut out target areas including a safety margin so no target spectra remain in the data set to be confused with false alarms. The simulated columns are appended to the right of the flight line.

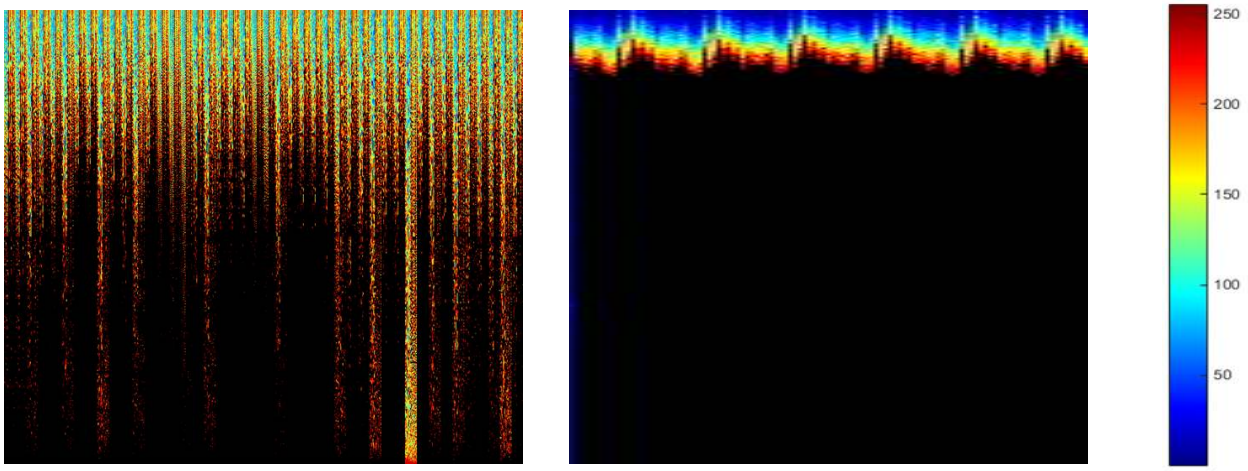

Figure 4. Result of ACE classification for the simulated mixtures of *Camouflage 1* in VNIR (left) and SWIR (right). The mixtures have a ratio of 100 % target at the bottom and are linearly reduced to 0 % at the top. Similarity is color-coded using the jet colormap and the similarities range from dark blue (no similarity and a value of 0) to black (perfect match and a value of 255). The different image resolutions are a result of the reduced amount of available test spectra in the SWIR data.

look identical for higher target ratios but start to look different once the variation of the background comes into play.

Image statistics for the ACE, GLRT, MF and CEM classifiers were taken from the same data sets that were used for the simulation, but with the target areas cut out. In a practical environment camouflaged targets are usually small enough to have a negligible effect on image statistics. When the statistics mirror the target spectrum, detection results are considerably lower.

4. RESULTS

The results for detection limits were computed using the seven classifiers from section 2. Background and target areas were manually selected from three VNIR and two SWIR data sets. Overall 19 target and 12 background areas were identified from the region depicted by Figures 1 and 2. The rectangles in the figures mark the areas with camouflage nets and molton.

The mean spectrum of each target area was used as a reference for classification. For the final results the mean detection limits of the two different models of camouflage nets were calculated. The results were calculated for each combination of target and background and are listed in Table 1 for the VNIR and Table 2 for the SWIR data. Each result represents the mean target fraction at 1 % false alarms for a given combination. In the tables

only the results of the best algorithm are displayed. Only the algorithms from Chapter 2 were used. None required more information than target and background spectra and no spatial relationships between neighboring pixels were exploited.
Table 3 contains the difference between VNIR and SWIR results and can be used to determine combinations that are easier to detect with a specific sensor. As Table 3 does not account for spatial resolution, Table 4 contains the VNIR/SWIR ratio. Depending on the ratio of spatial resolution between the sensors this can also be used to determine the suitability of a specific sensor type for certain expected combinations.
Notable differences are *Molton (black)* and *Camouflage 1* where SWIR data worked much better. The similarities in the simulated data for *Camouflage 1* mixed with *Asphalt* for both sensors at 1 % false alarms are depicted in Figure 4. Black values signify high similarity to the *Camouflage 1* reference spectrum. The detection limit in SWIR data is much better and the variance is significantly lower compared to VNIR results.

5. DISCUSSION

The results from Tables 1, 2 and 3 show that spectral signatures of target and background affect how robust the classifier will be. Generally, darker targets like the camouflage nets, *Tank* and *Decoy* are harder to detect for the classifiers. *Molton (black)* performed especially weak as it has almost no discernible features in the VNIR domain. It required a mean coverage of 0.9842 of a pixel in the VNIR data but only a coverage of 0.0452 in the SWIR data. Similarly, we discovered that the darker the background the better the detection limit gets. This can be seen when comparing the results of long and short grass to wet grass, the latter were generally better. The same holds for mixtures with *Tree (dark)* and *Tree (bright)*.
Comparing the results of *Molton (black)*, *Molton (grey)* and *Molton (white)*, the brightness in the VNIR roughly specifies the detection limit. Comparing the results in Table 1 there is approximately a factor $9 - 10$ difference between consecutive brightness levels. Considering the SWIR results *Molton (white)* and *Molton (grey)* almost have the same detection limit, *Molton (black)* is only slightly worse. Although the norm of the material spectra in the SWIR wavelength range are not equal, molton has some specific features that make it easier to discriminate from the background compared to the VNIR range.
Other major differences between the VNIR and SWIR data can be seen for the *Tank*, *Decoy* and *Camouflage 1* target. Using SWIR data the detection limit improves by 0.3259, 0.1818 and 0.1686 fraction of pixel size respectively. There was no configuration among our materials where classification of the VNIR data expressed a notable improvement in the detection limit.
However, all these results do not take the spatial resolution into account. As the spatial resolution of VNIR was twice as good as SWIR, calculating the ratio VNIR/SWIR per result can be seen in Table 4. As the area of a SWIR pixel is $2^2 = 4$ times the size of a VNIR pixel, only the results of *Molton (black)*, *Molton (grey)* and *Camouflage 1* benefit from SWIR data. The spatial resolution ratio may be different for other sensors. When SWIR sensors with better spatial resolution are available, other target materials like *Tank* and *Decoy* may be added to the list of targets that are easier to detect in SWIR data. However, *Camouflage 2)* and *Camouflage 2 (wet)* were easier to detect in the VNIR data. We assume that the increased availability of sensors for non-visible domains also lead to the necessity of specifically designed camouflage materials.
It is not surprising that the SAM classifier generally produced the worst results. It does not utilize image or background statistics. Surprisingly, OSP did not perform very well either, although it is the only algorithm in our test that uses background spectra to better discriminate between target and background. A reason for this may be the fact that not all materials from the scene were represented by the background library we used for the simulation. When looking at the image of false alarms it appears that mostly shadow areas and objects like cars or roof material that were not represented by the background library were detected. ACE, CEM, GLRT and MF all use the inverse covariance statistic of the data set and perform very similarly. In 71.3 % of all cases ACE produced the best results, followed by CEM with 18.4 %. However, the detection limits for ACE, CEM, MF and GLRT were very similar in all cases and when ACE was not the best algorithm it was usually second best. As the results of these four classifiers were so similar, using ACE when no additional information except the target signature is known seems like a good first approach. SAM, SID and OSP did not perform very well. The cases where one of these algorithms yielded the best results were those that have very low detection limits, like *Molton (black)* or *Camouflage 1* in the VNIR data.

Table 1. Mean detection limit for VNIR data. Results are given as fraction of pixel size covered by the target.

		background									
		Asphalt	Cement	Pavement	Dirt track	Grass (short)	Grass (long)	Grass (wet)	Tree (bright)	Tree (dark)	mean
target	Tank	0.5372	0.4831	0.5779	0.6273	0.6628	0.6212	0.5535	0.5334	0.2563	0.5392
	Decoy	0.3691	0.3355	0.4091	0.3953	0.4882	0.3685	0.3583	0.3159	0.1796	0.3577
	Molton (black)	0.9882	0.9782	0.9898	0.9880	0.9918	0.9905	0.9863	0.9837	0.9616	0.9842
	Molton (grey)	0.0703	0.1003	0.1205	0.1057	0.1176	0.0719	0.1054	0.0760	0.0590	0.0919
	Molton (white)	0.0111	0.0132	0.0158	0.0175	0.0178	0.0108	0.0166	0.0117	0.0104	0.0139
	Molton (green)	0.0162	0.0136	0.0126	0.0140	0.0100	0.0123	0.0066	0.0139	0.0107	0.0122
	Camouflage 1	0.2324	0.2589	0.2562	0.2383	0.2480	0.2237	0.1830	0.2151	0.1076	0.2181
	Camouflage 2	0.1799	0.1645	0.1536	0.1470	0.1333	0.1536	0.0634	0.1548	0.1116	0.1402
	Camouflage 2 (wet)	0.1870	0.1465	0.1402	0.1513	0.1467	0.1464	0.0577	0.1463	0.1022	0.1360

Table 2. Mean detection limit for SWIR data. Results are given as fraction of pixel size covered by the target.

		background									
		Asphalt	Cement	Pavement	Dirt track	Grass (short)	Grass (long)	Grass (wet)	Tree (bright)	Tree (dark)	mean
target	Tank	0.1796	0.2610	0.2474	0.1500	0.2038	0.2532	0.1760	0.2319	0.2161	0.2132
	Decoy	0.1432	0.2239	0.1980	0.1430	0.1844	0.1877	0.1696	0.1758	0.1576	0.1759
	Molton (black)	0.0236	0.0755	0.0586	0.0436	0.0511	0.0400	0.0244	0.0469	0.0431	0.0452
	Molton (grey)	0.0219	0.0360	0.0345	0.0115	0.0242	0.0234	0.0224	0.0287	0.0248	0.0253
	Molton (white)	0.0276	0.0354	0.0349	0.0082	0.0334	0.0266	0.0227	0.0303	0.0259	0.0272
	Molton (green)	0.0254	0.0359	0.0359	0.0135	0.0344	0.0246	0.0284	0.0305	0.0277	0.0285
	Camouflage 1	0.0351	0.0753	0.0708	0.0373	0.0455	0.0448	0.0471	0.0500	0.0402	0.0496
	Camouflage 2	0.0475	0.2121	0.2021	0.1698	0.1003	0.1872	0.1942	0.1971	0.2031	0.1682
	Camouflage 2 (wet)	0.0708	0.2235	0.1741	0.2221	0.1864	0.2466	0.1690	0.2390	0.2404	0.1969

Table 3. Difference of mean detection limits for SWIR and VNIR data. Differences are determined by VNIR - SWIR.

		background									
		Asphalt	Cement	Pavement	Dirt track	Grass (short)	Grass (long)	Grass (wet)	Tree (bright)	Tree (dark)	mean
target	Tank	-0.3576	-0.2221	-0.3304	-0.4772	-0.4590	-0.3679	-0.3775	-0.3015	-0.0401	-0.3259
	Decoy	-0.2259	-0.1116	-0.2111	-0.2523	-0.3038	-0.1807	-0.1887	-0.1400	-0.0220	-0.1818
	Molton (black)	-0.9646	-0.9027	-0.9311	-0.9444	-0.9407	-0.9505	-0.9618	-0.9368	-0.9185	-0.9390
	Molton (grey)	-0.0485	-0.0644	-0.0860	-0.0942	-0.0934	-0.0485	-0.0829	-0.0473	-0.0342	-0.0666
	Molton (white)	0.0165	0.0222	0.0192	-0.0093	0.0156	0.0158	0.0061	0.0187	0.0155	0.0134
	Molton (green)	0.0092	0.0223	0.0233	-0.0005	0.0244	0.0123	0.0219	0.0166	0.0170	0.0163
	Camouflage 1	-0.1973	-0.1836	-0.1854	-0.2010	-0.2026	-0.1789	-0.1359	-0.1651	-0.0674	-0.1686
	Camouflage 2	-0.1324	0.0477	0.0486	0.0228	-0.0330	0.0337	0.1308	0.0424	0.0915	0.0280
	Camouflage 2 (wet)	-0.1162	0.0771	0.0339	0.0708	0.0398	0.1002	0.1113	0.0927	0.1382	0.0609

Table 4. VNIR/SWIR ratio to determine resolution dependent suitability of different wavelength intervals.

		background									
		Asphalt	Cement	Pavement	Dirt track	Grass (short)	Grass (long)	Grass (wet)	Tree (bright)	Tree (dark)	mean
target	Tank	2.9912	1.8510	2.3354	4.1813	3.2518	2.4530	3.1447	2.3000	1.1856	2.6327
	Decoy	2.5770	1.4986	2.0659	2.7649	2.6470	1.9627	2.1127	1.7965	1.1395	2.0628
	Molton (black)	41.8579	12.9520	16.8775	22.6445	19.3968	24.7871	40.3852	20.9703	22.3046	24.6862
	Molton (grey)	3.2182	2.7902	3.4945	9.1911	4.8614	3.0750	4.6949	2.6464	2.3789	4.0390
	Molton (white)	0.4015	0.3735	0.4514	2.1377	0.5334	0.4052	0.7315	0.3845	0.4000	0.6465
	Molton (green)	0.6383	0.3785	0.3499	1.0400	0.2906	0.4996	0.2306	0.4560	0.3861	0.4744
	Camouflage 1	6.6756	3.9040	4.1342	6.9043	5.9865	5.4900	4.5286	4.8899	3.3531	5.0962
	Camouflage 2	3.8540	0.7737	0.7539	0.8689	1.3644	0.8396	0.3286	0.8011	0.5538	1.1265
	Camouflage 2 (wet)	2.6420	0.6552	0.8051	0.6811	0.7867	0.5936	0.3414	0.6120	0.4251	0.8380

6. OUTLOOK

Once target and background ROIs are selected the remaining analysis can be performed automatically. It is possible to test other combinations of targets on background materials very quickly in the future. A transfer of these results to generalize statements of detection limits for other weather and illumination conditions is of interest. Further analysis of the influence of illumination conditions on the target detection limits is required. During the next measurement campaigns it is planned to place target materials in the shadow of a building. Also, the effects of adjacency and multiple reflections need to be addressed. Especially camouflage nets are usually placed among vegetation and not placed directly on the grass. It remains to be tested if the approximated detection limits hold when the nets are partially concealed by vegetation. Also, the effect of sensor point spread function on the detection limits needs to be analyzed.

When the target material of interest is known, multiple procedures can improve the classification by selecting only a suitable subset of bands[8] or transforming the data to make it more robust against changes in illumination and material variation.[9] Data transformation techniques, like Principal Component Analysis[10] or Minimum Noise Fraction Transformation,[11] can also influence the detection limit. Further analysis is required.
Eventually, other methods to target and background simulation are proposed by Cohen[12] and Guanter[13] that can be tested to determine the robustness of the approximated detection limits.
Using spectral unmixing to quantify detection results might also be an interesting approach to find small fractions of a target in a big data set. However, only a few publications exist where the accuracy of unmixing algorithms is analyzed.[14] Furthermore, unmixing requires complete knowledge of the materials in the scene, similar to OSP, which is hard to come by especially in military scenarios.
Finally, a correlation between detection limit and spectral similarity between target and background is of interest to predict detection limits for unavailable target/background combinations.

ACKNOWLEDGMENTS

This research was supported by WTD 81 - Wehrtechnische Dienststelle für Informationstechnologie und Elektronik; Eidgenössisches Departement für Verteidigung, Bevölkerungsschutz und Sport VBS armasuisse Wissenschaft + Technologie; WTD 52 - Wehrtechnische Dienststelle für Schutz- und Sondertechnik. We thank our colleagues from Fraunhofer IOSB and University of Zurich who provided insight and expertise that greatly assisted the research.

REFERENCES

1. S. McCloskey, Y. Ding, and J. Yu, "Design and estimation of coded exposure point spread functions," *Pattern Analysis and Machine Intelligence, IEEE Transactions on* **34**, pp. 2071–2077, Oct 2012.
2. J. P. Kerekes, K. Ludgate, A. Giannandrea, N. G. Raqueno, and D. S. Goldberg, "Share 2012: subpixel detection and unmixing experiments," *Proc. SPIE* **8743**, pp. 1–7, 2013.
3. F. Kruse, A. Lefkoff, J. Boardman, K. Heidebrecht, A. Shapiro, P. Barloon, and A. Goetz, "The spectral image processing system (sips) - interactive visualization and analysis of imaging spectrometer data," *Remote Sensing of the Environment* **44**, pp. 145–163, 1993.
4. X. Jin, S. Paswater, and H. Cline, "A comparative study of target detection algorithms for hyperspectral imagery," in *SPIE Algorithms and Technologies for Multispectral, Hyperspectral, and Ultraspectral Imagery XV*, *Proc. SPIE* **7334**, pp. 1–12, 2009.
5. T. Ayoub and A. Haimovich, "Modified glrt signal detection algorithm," *Aerospace and Electronic Systems, IEEE Transactions on* **36**, pp. 810–818, Jul 2000.
6. L. L. Scharf and B. Friedlander, "Matched subspace detectors," *Signal Processing, IEEE Transactions on* **42**, pp. 2146–2157, Aug 1994.
7. C.-I. Chang, "Spectral information divergence for hyperspectral image analysis," in *Geoscience and Remote Sensing Symposium, 1999. IGARSS '99 Proceedings. IEEE 1999 International*, **1**, pp. 509–511 vol.1, 1999.
8. J. Maerker, W. Gross, W. Middelmann, and A. Ebert, "Hyperspectral band selection using statistical models," *SPIE Algorithms and Technologies for Multispectral, Hyperspectral, and Ultraspectral Imagery XVII* **8048**, 2011.
9. W. Gross, G. Keskin, H. Schilling, A. Lenz, and W. Middelmann, "Automatic modeling of nonlinear signal source variations in hyperspectral data," in *Geoscience and Remote Sensing Symposium (IGARSS), 2014 IEEE International*, pp. 2965–2968, July 2014.
10. H. Abdi and L. J. Williams, "Principal component analysis," *Wiley Interdisciplinary Reviews: Computational Statistics* **2**(4), pp. 433–459, 2010.
11. A. Green, M. Berman, P. Switzer, and M. Craig, "A transformation for ordering multispectral data in terms of image quality with implications for noise removal," *IEEE Transactions on Geoscience and Remote Sensing* **26**, pp. 65–74, (1988).
12. Y. Cohen, Y. August, D. G. Blumberg, and S. R. Rotman, "Evaluating subpixel target detection algorithms in hyperspectral imagery," *Journal of Electrical and Computer Engineering* **2012**, p. 15, 2012.

13. L. Guanter, K. Segl, and H. Kaufmann, "Simulation of optical remote-sensing scenes with application to the enmap hyperspectral mission," *Geoscience and Remote Sensing, IEEE Transactions on* **47**, pp. 2340–2351, July 2009.
14. W. Gross, S. Borchardt, and W. Middelmann, "Evaluation of spectral unmixing using nonnegative matrix factorization on stationary hyperspectral sensor data of specifically prepared rock and mineral mixtures," *OCM 2013 - Optical Characterization of Materials - conference proceedings* **1**, pp. 169–178, 2013.